PAPER

Check for updates

Magneto-mechanical destruction of cancer-associated fibroblasts using ultra-small iron oxide nanoparticles and low frequency rotating magnetic fields†

Sara Lopez,‡[ab] Nicolas Hallali,‡[a] Yoann Lalatonne, [ID] ‡[cd] Arnaud Hillion,[a] Joana C. Antunes,[c] Nizar Serhan,[ab] Pascal Clerc,[ab] Daniel Fourmy,[ab] Laurence Motte,‡*[c] Julian Carrey‡*[a] and Véronique Gigoux [ID] ‡*[ab]

The destruction of cells using the mechanical activation of magnetic nanoparticles with low-frequency magnetic fields constitutes a recent and interesting approach in cancer therapy. Here, we showed that superparamagnetic iron oxide nanoparticles as small as 6 nm were able to induce the death of pancreatic cancer-associated fibroblasts, chosen as a model. An exhaustive screening of the amplitude, frequency, and type (alternating *vs.* rotating) of magnetic field demonstrated that the best efficacy was obtained for a rotating low-amplitude low-frequency magnetic field (1 Hz and 40 mT), reaching a 34% ratio in cell death induction; interestingly, the cell death was not maximized for the largest amplitudes of the magnetic field. State-of-the-art kinetic Monte-Carlo simulations able to calculate the torque undergone by assemblies of magnetic nanoparticles explained these features and were in agreement with cell death experiments. Simulations showed that the force generated by the nanoparticles once internalized inside the lysosome was around 3 pN, which is in principle not large enough to induce direct membrane disruption. Other biological mechanisms were explored to explain cell death: the mechanical activation of magnetic nanoparticles induced lysosome membrane permeabilization and the release of the lysosome content and cell death was mediated through a lysosomal pathway depending on cathepsin-B activity. Finally, we showed that repeated rotating magnetic field exposure halted drastically the cell proliferation. This study established a proof-of-concept that ultra-small nanoparticles can disrupt the tumor microenvironment through mechanical forces generated by mechanical activation of magnetic nanoparticles upon low-frequency rotating magnetic field exposure, opening new opportunities for cancer therapy.

Introduction

Iron oxide magnetic nanoparticles (IONPs), which display low toxicity and good biocompatibility in humans, are the subject of renewed interest in the field of cancer nanotherapy.[1] Over the past few decades, a wide range of IONPs of controlled size, composition and functionality have been developed, providing an excellent resource for nanomedicine. Indeed, they have been already approved for clinical use as a contrast agent for magnetic resonance imaging and as an iron supplement for the treatment of iron deficiency anemia.[2,3] When exposed to a high-frequency alternating magnetic field, IONPs release heat which can be used to develop biological approaches such as the eradication of cancer cells (magnetic hyperthermia),[4–8] on-demand drug release,[9] the stimulation of neurons,[10] the induction of gene expression[11] or the disruption of the extra-cellular matrix of the tumor microenvironment.[12,13] In particular, magnetic hyperthermia has been the subject of active research activity in the past few decades and tremendous progress has been made in basic research on this promising cancer treatment.[14] Magnetic hyperthermia using IONPs under a high-frequency alternating magnetic field has distinctive benefits for tumor ablation in deep tissues because of the

[a]*Laboratoire de Physique et Chimie des Nano-Objets (LPCNO), CNRS-UPS-INSA UMR5215, 135 Avenue de Rangueil, F-31077 Toulouse, France. E-mail: julian.carrey@insa-toulouse.fr*

[b]*INSERM ERL1226, Receptology and Targeted Therapy of Cancers, 1 Avenue du Professeur Jean Poulhes, F-31432 Toulouse, France. E-mail: veronique.gigoux@inserm.fr*

[c]*Université Sorbonne Paris Nord, Laboratory for Vascular Translational Science, LVTS, INSERM, UMR 1148, F-93000 Bobigny, France. E-mail: laurence.motte@sorbonne-paris-nord.fr*

[d]*Services de Biochimie et Médecine Nucléaire, Hôpital Avicenne Assistance Publique-Hôpitaux de Paris, F-93009 Bobigny, France*

† Electronic supplementary information (ESI) available. See DOI: 10.1039/d1na00474c

‡ Equal participation.

convenience of distant control and manipulation by the magnetic field. However, this approach, requiring magnetic fields with frequencies ranging from tens of kHz to MHz, generates eddy currents inside healthy tissues that may cause patient discomfort and adverse effects. But above all, applying high-frequency magnetic fields on a large scale (humans) remains a technical challenge, because of the strong heating of coils and magnetic cores under such magnetic fields.[15] Consequently, only a few clinical trials have been performed applying a magnetic field with a moderate frequency and amplitude (100 kHz and 20 mT) which caused several adverse effects due to heat diffusion to surrounding tissues and presented limiting factors such as irregular intra-tumoral heat distribution.[16,17]

Recent reports highlighted new potentialities of IONPs for anti-cancer therapy.[18] When exposed to low-frequency magnetic fields, IONPs generate mechanical forces and torques, which are transmitted to materials they are in contact with. Such torques can be used to control the calcium entry within cells, improve gene transfection or tissue engineering, manipulate molecules, stimulate drug release, induce protein degradation, activate enzymes or destroy cancer cells.[19–24] The proof-of-concept of *in vitro* and *in vivo* targeting by the IONPs of tumors overexpressing surface receptors could, moreover, allow it without any invasive intra-tumoral injections.[25,26] This new approach could solve the problems related to magnetic hyperthermia mentioned above and would be highly beneficial to IONP-based anti-cancer therapy by offering a new opportunity to treat cancer. Several studies have already demonstrated that micrometric discs, spheres, or wires induce the death of cancer cells under low-frequency alternating (AMF) or rotating (RMF) magnetic fields.[27–30] So far, some studies have reported the death of cancer cells using IONPs exposed to AMF or RMF.[31–41] But they did not explore stringently, theoretically as well as experimentally, for optimal magnetic field parameters – *e.g.*, type, amplitude, and frequency – able to induce torque leading to cell damages.

Several mechanisms protect a tumor against potential treatments. One of them is the tumoral microenvironment which creates a supportive scaffold for tumor cell proliferation and a barrier limiting the penetration and the dispersion of chemotherapeutic treatments into the tumor. Cancer-associated fibroblasts (CAFs) are the key components of the tumor microenvironment, since they actively deposit an extracellular matrix (ECM), by producing and secreting abundantly ECM proteins including types I and III collagen, that prevent chemotherapeutic drugs from reaching their target.[42] Moreover, CAFs secrete factors in the extracellular medium (hormones, growth factors, chemokines…), promoting tumor growth and participating in the resistance acquisition of cancer cells to anti-cancer treatments such as in pancreatic cancer.[43,44] Among the precision nanotherapies aiming to deliver nanoparticles inside the tumor as a way of cancer control, the therapeutic targeting of CAFs using nano-agents thus constitute a new interesting strategy compared to main studies taking care of cancer cells.

In the present work, we develop a strategy targeting and killing CAFs by remote magneto-mechanical destruction. Interestingly, we show that it is possible to do it using nanoparticles as small as 6 nm, a puzzling result since the forces generated by such ultra-small MNPs are expected to be too small to disrupt cell membranes. We explain the origin of the observed effect and its magnetic field dependence using state-of-the-art magnetic simulations and shed light on cell death mechanisms. These data are very promising and show that ultra-small nanoparticles targeting lysosomes hold the potential for remote magneto-mechanical destruction of cells by disrupting their lysosomes, thus offering a new promising therapeutic strategy against tumors.

Results

USPION@gastrin and specific CAF targeting

We first developed and characterized ultra-small superparamagnetic iron oxide nanoparticles (USPIONs) targeting pancreatic CAFs, chosen as a model. Then, we analyzed their uptake by pancreatic CAFs as well as their subcellular localization. 6 nm USPIONs were synthesized using a microwave nonaqueous sol–gel method.[45] As shown in previous studies, the USPION surface has to be functionalized in order to obtain biostability and biocompatibility and to allow specific targeting. Herein, the USPION surface was functionalized with phosphonate pegylated ligands bearing carboxylate functions as the terminal group (PO–PEG–COOH). The phosphonate group shows high affinity for the metal oxide surface whereas carboxylate groups could be used in a second step for covalent coupling of targeting molecules.[26] The magnetic core size, measured by TEM, equaled 6.0 ± 1.3 nm (Fig. 1a). The average number of PO–PEG–COOH per nanoparticle, evaluated using Fourier transform infrared spectroscopy, was 176 ± 16 (ESI Fig. S1†). The hydrodynamic diameter in the culture medium containing 0.5% FBS was found to be equal to 20.6 ± 2.6 nm, indicating low aggregation (Fig. 1b). As expected, 6 nm USPIONs exhibited a saturation magnetization of 65.6 ± 1.8 A m^2 kg^{-1} Fe (Fig. 1c).[46] 6 nm USPIONs were then decorated with a fluorophore (DY647), allowing their fluorescence emission detection, and with a synthetic peptide analog of gastrin, to selectively target pancreatic CAFs expressing the type 2 cholecystokinin receptor (CCK2R). The analysis by DLS, in a biological medium enriched with 0.5% FBS, showed a distribution of the functionalized 6 nm USPIONs, called USPION@gastrin, of around 43 ± 4 nm (Fig. 1b). OPA assay indicates an average number of 26 peptides per nanoparticle using the gastrin peptide calibration curve (Fig. S2†).

The cancer progression and aggressiveness are not only dictated by the tumor cells, but also involve the tumor microenvironment. In some types of cancer, the microenvironment may account for the largest portion of the tumor, such as in pancreatic adenocarcinoma whose stroma accounts for up to 80% of the tumor mass. Moreover, the tumoral microenvironment constitutes a physical barrier limiting drug penetration and participates in the drug resistance acquisition by the tumor. Among the cells constituting the tumor microenvironment, CAFs deposit an extracellular matrix and promote tumor growth and resistance acquisition of tumors. Here, we developed a nanotherapeutic strategy targeting the pro-tumoral CAFs
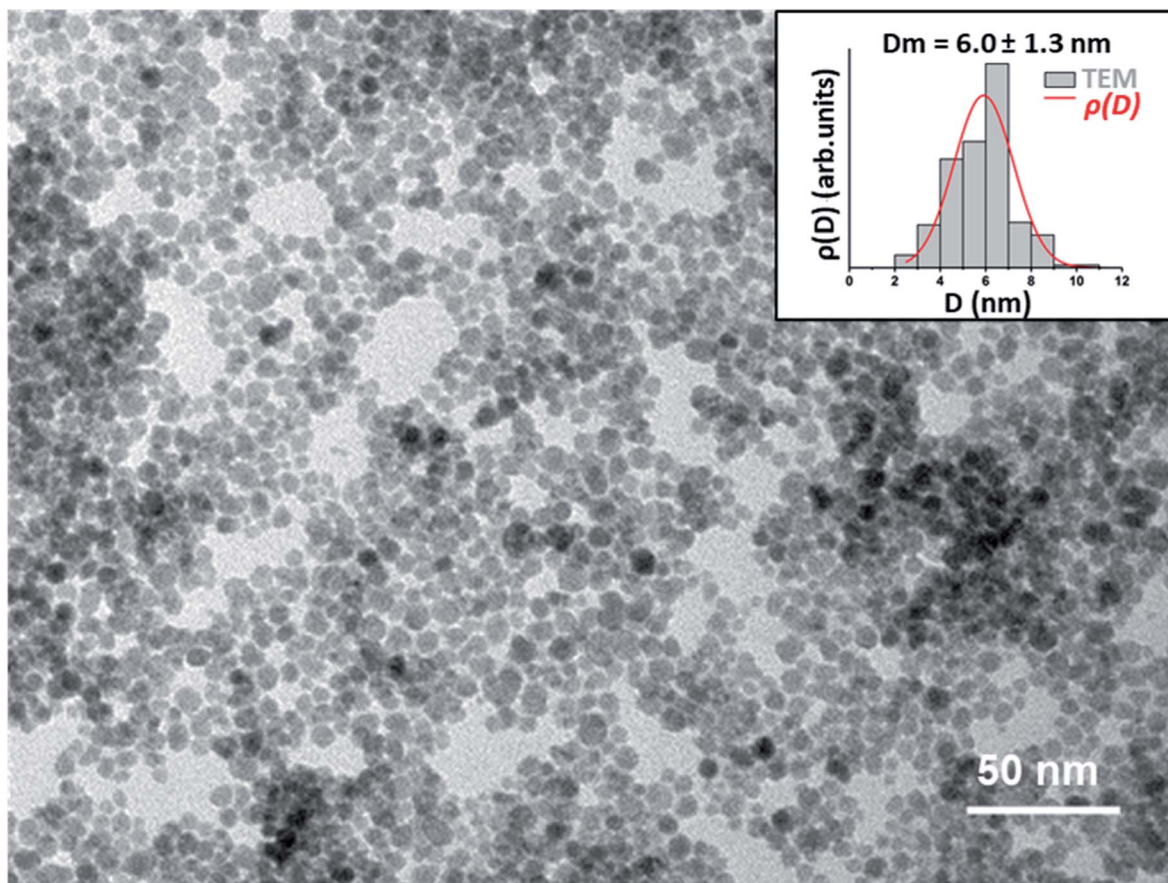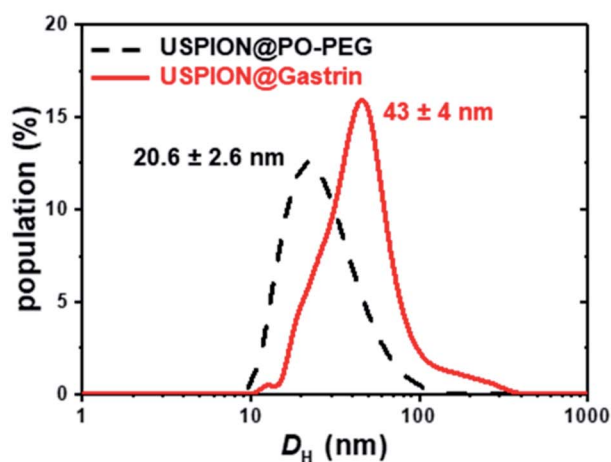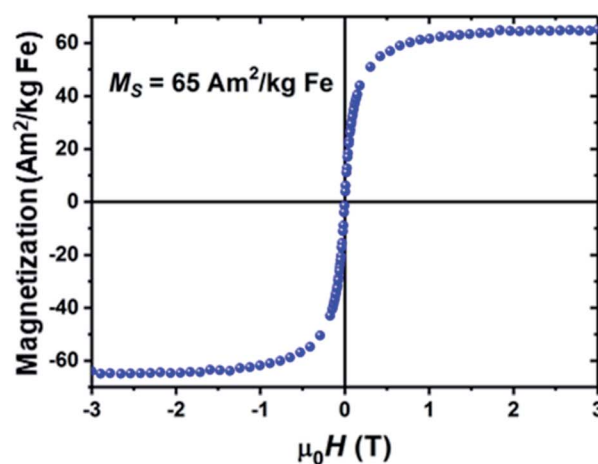
Fig. 1 (a) TEM image of 6 nm USPION@PO-PEG; (inset) particle size distribution deduced from TEM observations (bars) and fit of the size distribution (line); (b) hydrodynamic particle size distribution before (dashed black) and after functionalization with gastrin (full red) measured in volume by dynamic light scattering; (c) hysteresis loop of 6 nm USPION@PO–PEG measured at 300 K.

of pancreatic adenocarcinoma, chosen as a model because pancreatic adenocarcinoma is a typical fibrotic tumor composed of up to 80% of its volume a stiff stroma, for which CAFs play a critical role in invasion and chemoresistance.[44] The type 2 cholecystokinin receptor, CCK2R, was shown to be expressed on cancer-associated fibroblasts (CAFs) in pancreatic

adenocarcinoma. Moreover, its targeting, using an antagonist, inhibits the secretion of collagen, reduces fibrosis in the tumor microenvironment and halts the cancer progression, making the CCK2R a good candidate for pancreatic cancer pro-tumoral CAF targeting.[47–49] The tumor microenvironment targeting strategy elaborated in this study requires a specific recognition of pancreatic CAFs expressing the CCK2R by USPION@gastrin. We analyzed the CCK2R expression in two immortalized human CAF cell lines, called CAF1 and CAF2, isolated from the resected pancreas tissue of two patients undergoing operation for pancreatic cancer. Unfortunately, these cell lines do not express the detectable level of the CCK2R (Fig. S3a†). We therefore elaborated pancreatic CAFs expressing the CCK2R by permanently transfecting the CAF1 and CAF2 cell lines with an expression vector coding for the human CCK2R; two CAF cell lines expressing the CCK2R were respectively selected and termed CAF1-CCK2 and CAF2-CCK2 (Fig. S3a†). Of note, the CAF2-CCK2 cell line expresses the CCK2R with a 3.7-fold lower level than the CAF1-CCK2 cell line.

We first characterized the binding properties and the uptake of USPION@gastrin (Fig. 2a–d). The kinetics of USPION@gastrin binding and internalization determined by flow cytometry indicate that the amount of USPION@gastrin taken up by CAF1-CCK2 and CAF2-CCK2 increased with the time of incubation and stabilized after 24 h incubation for CAF1-CCK2 and still increased continuously for CAF2-CCK2 (Fig. 2a). Furthermore, the amount of bound and internalized USPION@gastrin was higher and more rapid in CAF1-CCK2 cells than in CAF2-CCK2 cells, indicating that the USPION@gastrin uptake depends on the level of CCK2R expression at the cell surface. The global magnetic moment of Fe was evaluated by vibrating sample magnetometry as a quantitative method to measure magnetic nanoparticle quantity in cells (Fig. 2b). After 24 h of incubation, magnetic measurements showed an amount of 2.26 ± 0.33 and 1.60 ± 0.19 pg of magnetic Fe per CAF1-CCK2 or CAF2-CCK2 cell, confirming that the USPION@gastrin uptake depends on the level of CCK2R expression at the cell surface. The specificity of USPION@gastrin binding and internalization was then determined by flow cytometry after 24 h of incubation (Fig. 2c and d). The quantification of flow cytometry results indicated that the amount of USPION@gastrin taken up by CAF cells increased with the nanoparticle concentration and showed a highly specific
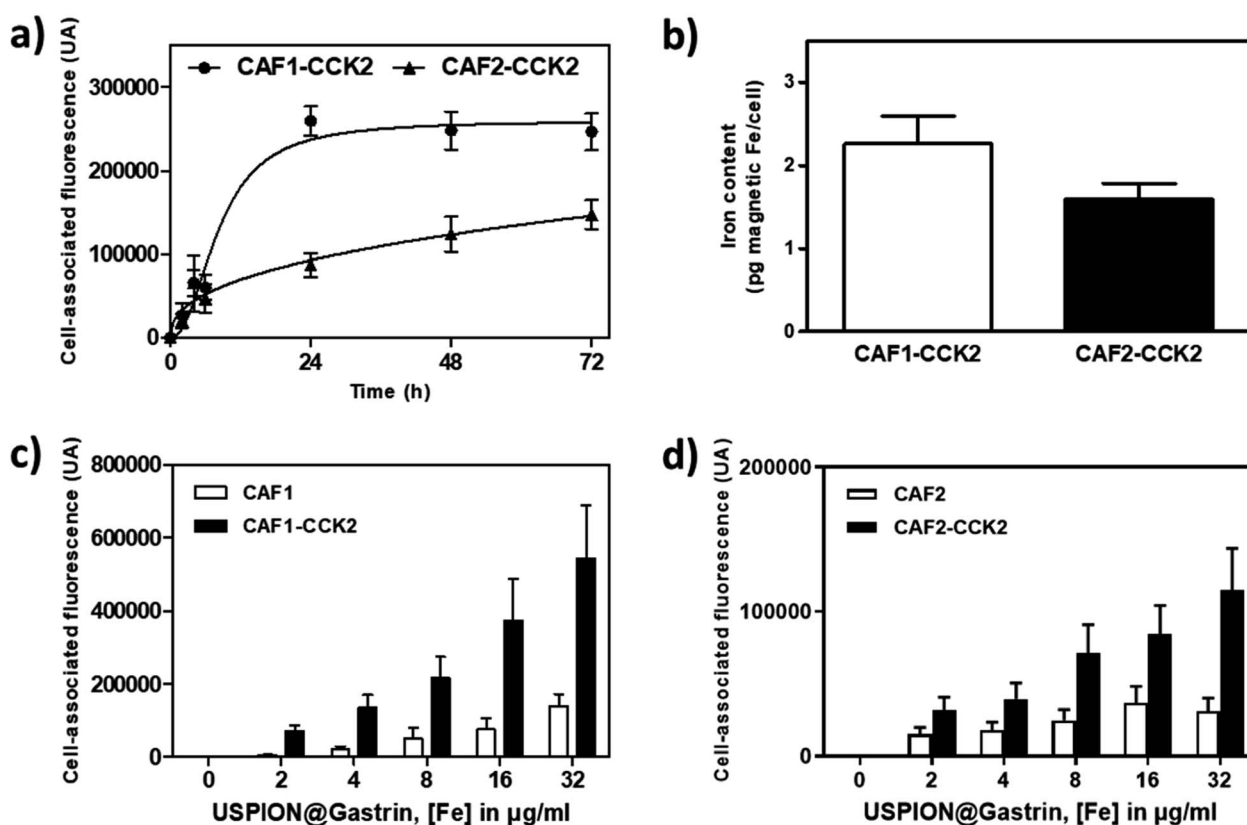

Fig. 2 USPION@gastrin specifically bind to CAF cells expressing the CCK2R, subsequently internalized and accumulated into lysosomes. (a) Kinetics of USPION@gastrin uptake by CAF1-CCK2 and CAF2-CCK2. Cells were incubated with 16 µg ml^{-1} of USPION@gastrin for 2, 4, 6, 24 h, 48 h and 72 h. Fluorescence was measured by flow cytometry, and the results are expressed as fluorescence associated with the cells and are the mean $\pm$ SEM of at least three separate experiments. (b) CAF1-CCK2 and CAF2-CCK2 cells were incubated with 16 µg ml^{-1} of USPION@gastrin for 24 h. Fe contained in superparamagnetic MNPs was measured by using a vibrating sample magnetometer. (c) and (d) USPION@gastrin uptake by CAF1 and CAF1-CCK2 (c) or CAF2 and CAF2-CCK2 (d) cells expressing or not the CCK2R. Cells were incubated with increased concentrations of USPION@gastrin for 24 h. Cell-associated fluorescence was measured by flow cytometry, and the results are expressed as fluorescence associated with the cells and are the mean $\pm$ SEM of at least three separate experiments.

targeting of CAFs expressing the CCK2R since USPION@gastrin was taken up in higher amounts by CAF1-CCK2 and CAF2-CCK2 cells compared to CAF1 and CAF2 cells lacking the CCK2R (Fig. 2c and d). Indeed, the uptake of USPION@gastrin by CAF1-CCK2 was 13.0 ± 0.1, 6.9 ± 1.2, 4.2 ± 1.4, 5.0 ± 1.0 or 3.9 ± 1.1 higher compared to CAF1 cells, at the low extracellular concentrations of USPION@gastrin corresponding to 2, 4, 8, 16 or 32 μg_{Fe} ml^{-1} (Fig. 2c). Similarly, the uptake by CAF2-CCK2 cells was 2.1 ± 0.6, 2.2 ± 0.7, 2.9 ± 0.8, 2.3 ± 0.7 or 3.7 ± 0.4 higher than in CAF2 cells at the same USPION@gastrin concentrations (Fig. 2d). Moreover, competition studies showed that an excess of gastrin inhibited the USPION@gastrin uptake by CAF1-CCK2 and CAF2-CCK2 cells (Fig. S3b and c†). These results indicate that CAFs overexpressing specific surface receptors can be effectively targeted with magnetic nanoparticles, and also validate the use of gastrin to target pancreatic CAFs expressing the CCK2R.

We next characterized the cellular fate of USPION@gastrin in the CAF cells (Fig. 3a–h). The transmission electron microscopy (TEM) images of CAF1-CCK2 and CAF2-CCK2 cells indicated that USPION@gastrin was mainly localized in lysosomes (Fig. 3a–d). Based on the TEM images, the concentration of NPs inside a lysosome was evaluated to be in the range of 500 to 5000 nanoparticles per lysosome while the volume concentration of USPION@gastrin in lysosomes was estimated to be

around 15%. A confocal microscopy study confirmed that USPION@gastrin accumulated in the lysosomal compartment of CAF cells expressing the CCK2R after 24 h of incubation, whereas they are poorly present in the lysosomes of CAF1 and CAF2 cells devoid of the CCK2R (Fig. 3e–h). Fig. 3e and f show that the USPION@gastrin internalization was respectively 5.1 ± 1.0 and 3.0 ± 0.3 more important in CAF1-CCK2 and CAF2-CCK2 cells than in CAF1 and CAF2 cells, in agreement with previous results obtained by flow cytometry analysis (Fig. 2c and d). The analysis of USPION@gastrin/Lysotracker colocalization demonstrated that 84.1 ± 1.1 and $90.6 \pm 1.1\%$ of USPION@gastrin taken up by cells were localized inside the lysosomes of CAF1-CCK2 and CAF2-CCK2 cells, respectively (Fig. 3g and h).

Torque undergone by an assembly of USPIONs

First, let us say a few words on the magnetic properties of the nanoparticles. In this type of nano-object, the anisotropy of individual particles comes from their shape, surface and magnetocrystalline anisotropy. At a diameter of 6 nm, they are expected to have single-crystal, single-domain and superparamagnetic characteristics at room temperature. When they are under the form of assemblies, anisotropy originating from collective effects and dipolar interactions between the single objects emerges. This leads to a ferromagnetic-like
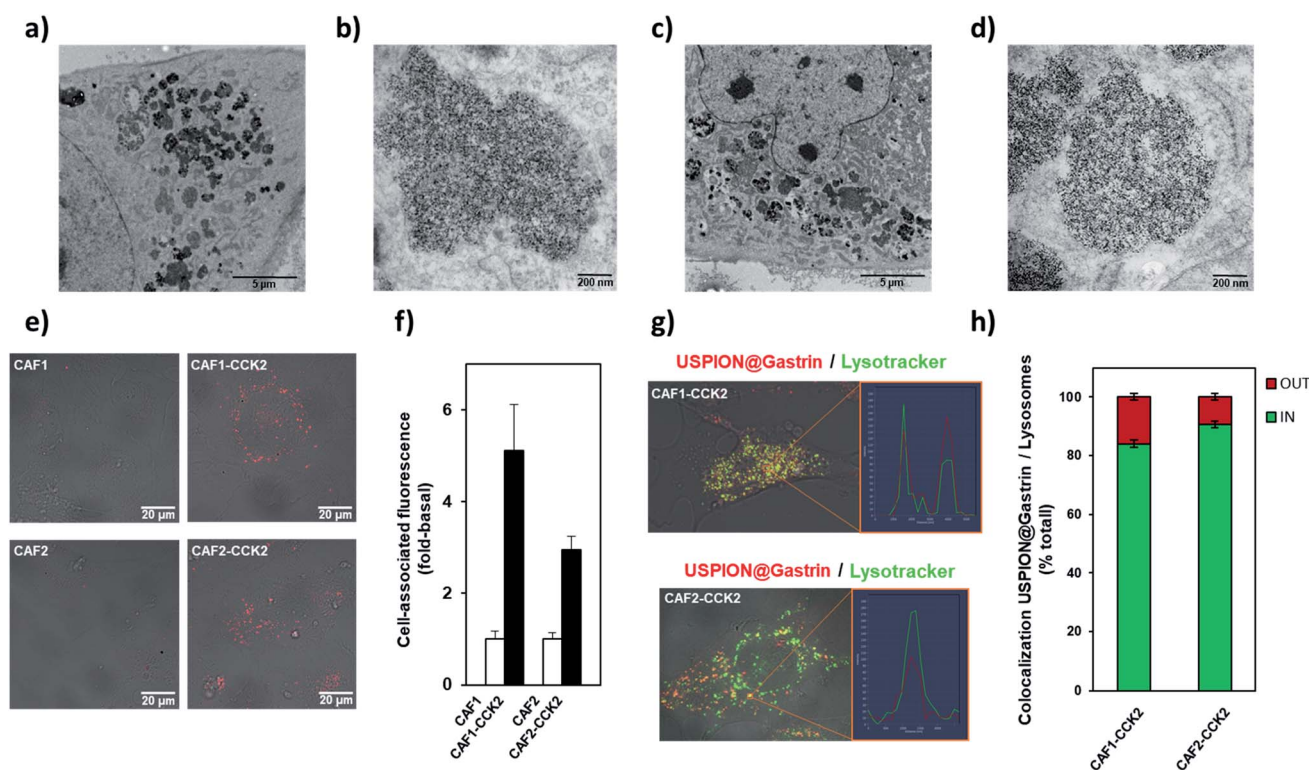

Fig. 3 Subcellular colocalization of USPION@gastrin. (a–d) Electron microscopy analysis of USPION@gastrin accumulation in CAF1-CCK2 and CAF2-CCK2 cells. CAF1-CCK2 and CAF2-CCK2 cells were incubated with 16 µg ml^{-1} of USPION@gastrin for 24 h. Image representative of USPION@gastrin accumulated in cells (a) and (c), and in lysosomes (b) and (d). (e and f) Analysis of USPION@gastrin localization by confocal microscopy. CAF1, CAF1-CCK2, CAF2 and CAF2-CCK2 cells were incubated with 16 µg ml^{-1} of USPION@gastrin for 24 h, and then observed by confocal microscopy (e). Quantification of USPION@gastrin uptake by the analysis of confocal microscopy images (f). CAF1-CCK2 and CAF2-CCK2 cells were incubated with 16 µg ml^{-1} of USPION@gastrin for 24 h, and then with 10 nM Lysotracker Green for 15 minutes and observed by confocal microscopy (g). Quantification of USPION@gastrin accumulation in lysosomes by the analysis of confocal microscopy images (h).

behaviour of the assemblies, which generates torques well above the one expected for non-interacting nanoparticles (see Fig. 14 and Discussion in ref. 50). In ref. 50, one can read that "*Everything happens as if large anisotropy NPs in the superparamagnetic regime in a given range of concentrations behave exactly as low anisotropy noninteracting ferromagnetic NPs.* » Quantitatively, the total torque τ of an assembly is expected to scale as $\tau = \tau_{ind}\sqrt{N}$, where τ_{ind} is the torque generated by a single particle and N the number of particles in the assembly. However, it is shown in ref. 50 that, under certain conditions, when the assembly presents a ferromagnetic-like behaviour, the torque can be larger at room temperature.

Fig. 4a illustrates the theoretical aspects related to the force generated by an assembly of USPIONs submitted to a rotating (RMF) or an alternating (AMF) magnetic field. Calculations have been performed for a nanoparticle diameter of 6 nm and using the magnetic parameters of magnetite (see the Methods; saturation magnetization $M_s = 500$ kA m^{-1} and anisotropy $K_{eff} = 13$ kJ m^{-3}). The experimental magnetization value 65 A m^2 kg^{-1} corresponds to 336 kA m^{-1}. Since the torque directly scales with the magnetization, the theoretical forces which will be presented below are reduced by approximately one third if the experimental value is used. The geometrical characteristics of the 6 nm USPION assembly were evaluated from TEM images to be as close as possible to the studied system: the number of particles N in the assembly, corresponding to the average number of particles in the lysosomes, was $N = 3000$ nanoparticles, with a volume concentration $c = 15\%$. First, the simulations showed that the force depends on the amplitude of the AMF: at lower amplitudes, the force increases with the field until it reaches a plateau of 0.7 pN for amplitudes larger than 100 mT. In contrast, the application of a RMF generates a strong torque peak, which occurs in a small range of field amplitudes (20–60 mT), a behaviour that is due to the breaking of time reversal symmetry when the magnetic field rotates, as described in a previous study.[50] Only in a small range of RMF amplitudes (30–60 mT), the generated forces are able to be above 1 pN, which is a lower limit to start breaking chemical and/or biological bonds.[18] The highest theoretical force occurs for a RMF of 50 mT and reaches 3 pN. With the amplitudes of RMF greater than 100 mT, the force reaches a plateau of 0.7 pN.

Induction of CAF death through low frequency rotating magnetic field actuation of USPION@gastrin

Based on the previously described simulations, we first screened the efficiency of different amplitudes (20 to 380 mT) and frequencies (0.2 to 20 Hz) of the rotating magnetic field (RMF) to induce the death of CAFs having accumulated USPION@gastrin inside their lysosomes. For this purpose, CAF1-CCK2 cells expressing a high level of the CCK2R were incubated with USPION@gastrin at 4, 8 or 16 μg$_{Fe}$ ml^{-1} for 24 h, washed to eliminate unbound and non-internalized USPION@gastrin and exposed to RMF for 2 h while temperature was maintained at 37 °C. Controls were composed of cells lacking USPION@gastrin and cells having internalized USPION@gastrin but that were not exposed to RMF. After RMF

exposure, the cells were cultured under standard conditions for recovery. The impact of treatment was determined by counting dead cells labeled with iFluor488-tagged annexin V (AnnV) and/or propidium iodide (PI) by flow cytometry, 4 h after RMF exposure (Fig. 4b, ESI Fig. S4–S8†). As shown in Fig. 4b, RMF application caused the cells having accumulated USPION@gastrin to die at most amplitudes and frequencies. Interestingly, the maximum effect was observed with a low frequency of 1 Hz and a small amplitude of 40 mT leading to the death of $17.9 \pm 3.0\%$ and $33.8 \pm 2.8\%$ of CAF1-CCK2 cells incubated with 8 or 16 μg$_{Fe}$ ml^{-1} of USPION@gastrin, respectively. This corresponds to a 3.0 ± 0.9- and 5.6 ± 1.7-fold increase in cell mortality ($p < 0.05$ and $P < 0.001$, Fig. 4c, ESI Fig. S4†). Similarly, the 1 Hz/40 mT RMF increased the cell mortality of CAF2-CCK2 cells incubated with 8 or 16 μg$_{Fe}$ ml^{-1} of USPION@gastrin by 2.2 ± 0.4- or 2.5 ± 0.2-fold respectively (dead cells: 14.0 ± 1.7 or $16.5 \pm 0.4\%$ of CAF2-CCK2 cells incubated with 8 or 16 μg$_{Fe}$ ml^{-1} of USPION@gastrin *vs.* $6.5 \pm 0.6\%$ CAF2-CCK2 cells lacking nanoparticles, $p < 0.001$, Fig. 4c). No significant effect was observed on CAF1-CCK2 and CAF2-CCK2 cells lacking USPION@gastrin and exposed to RMF whatever the amplitude and frequency used, as well as on CAF1-CCK2 and CAF2-CCK2 cells incubated with USPION@gastrin but not exposed to RMF (Fig. 4c, ESI Fig. S4–S8†). Superimposed on the simulations, the cell death rate obtained experimentally at different amplitudes of RMF showed that the shape of the curve followed closely the force generated by USPION assembly, indicating that experimental data of the RMF impact on cell death are in good agreement with the simulations of the magnetic torque (Fig. 4a).

To compare the impact of different types of magnetic fields, we then focused on the CAF1-CCK2 cell line, which presented a better response to RMF exposure. CAF1-CCK2 cells having accumulated USPION@gastrin within their lysosomes were exposed to a 40 mT static (SMF), a 40 mT/1 Hz rotating (RMF) or a 40 mT/1 Hz alternating (AMF) magnetic field. After magnetic field exposure, the cells were cultured under standard conditions for recovery. The impact of treatment was determined by counting dead cells labeled with iFluor488-tagged AnnV and/or PI by flow cytometry, 4 h after magnetic field exposure. As shown in Fig. 4d, a significant increase of cell death was observed when USPION@gastrin was submitted to a 40 mT/1 Hz RMF or AMF, whereas no significant effect was observed under a 40 mT SMF. Moreover, we demonstrate that RMF is the most efficient way to cause the death of cells having accumulated USPION@gastrin. Indeed, RMF caused the death of $17.9 \pm 3.0\%$ and $33.8 \pm 2.8\%$ of CAF1-CCK2 cells incubated respectively with 8 or 16 μg$_{Fe}$ ml^{-1} of USPION@gastrin, whereas AMF killed only $14.7 \pm 0.3\%$ CAF1-CCK2 cells ($p < 0.001$) incubated with 16 μg$_{Fe}$ ml^{-1} of USPION@gastrin. Of note, SMF, AMF or RMF did not affect the viability of cells devoid of USPION@gastrin.

Finally, we analyzed the effect of repeated RMF treatment on the cell proliferation of CAF1-CCK2 and CAF2-CCK2 cells (Fig. 4e and f). CAF1-CCK2 and CAF2-CCK2 were incubated with USPION@gastrin at 16 μg$_{Fe}$ ml^{-1} for 72 h, washed to eliminate unbound and non-internalized USPION@gastrin and exposed to RMF for 2 h once a day (from day 5 to 10) while temperature
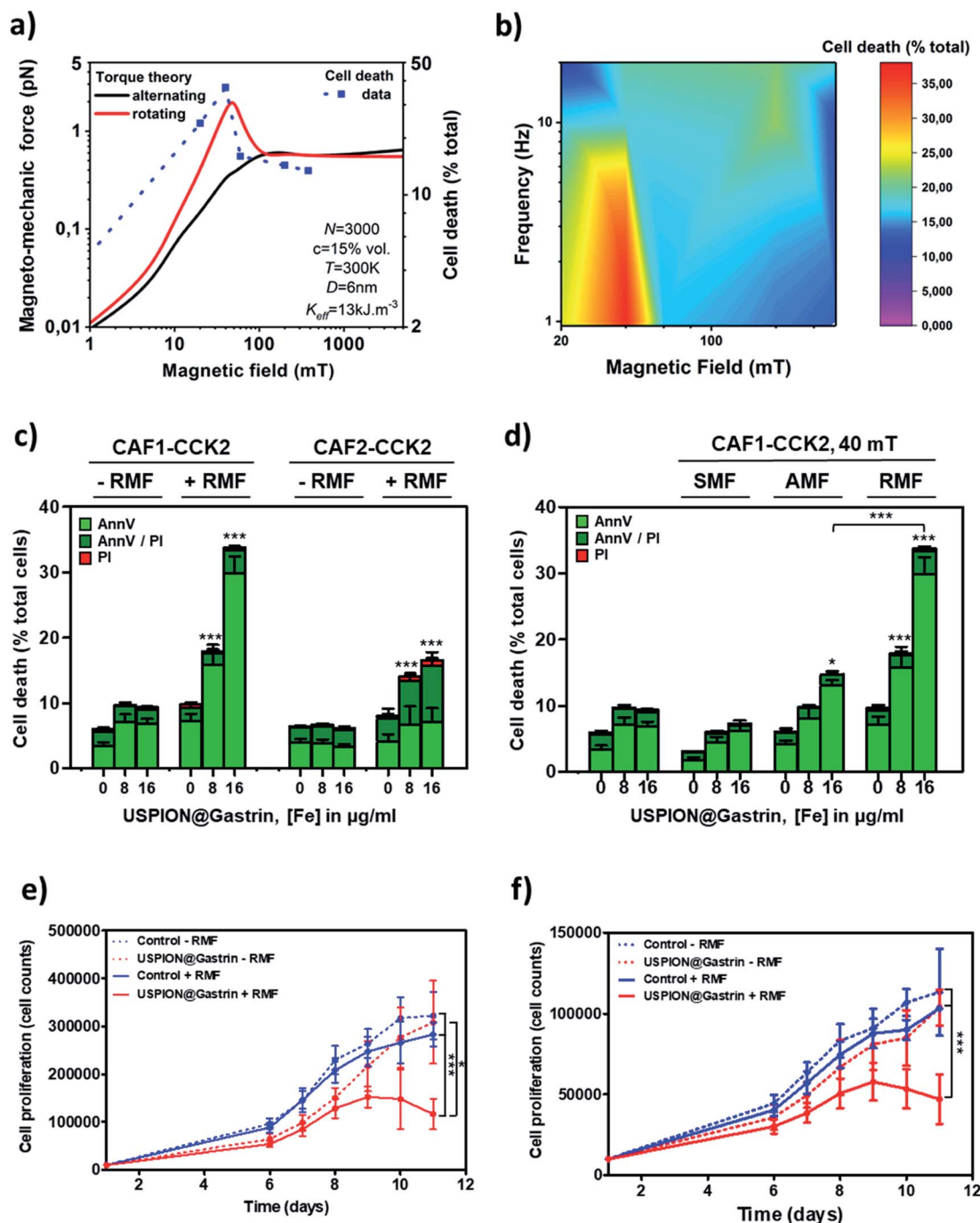
Fig. 4   USPION@gastrin generates a torque inducing the death of CAF-CCK2 cells under a low frequency rotating magnetic field. (a) Theoretical force generated by USPION@gastrin under AMF or RMF, compared to the evolution of CAF1-CCK2 cell death after RMF exposure experimentally obtained, for different amplitudes of the magnetic field. The force is calculated using monodisperse USPIONs of diameter $d = 6$ nm, with a uniaxial anisotropy $K_{eff} = 13$ kJ m^{-3} and is the one generated by the 3000 nanoparticle assembly at a volume concentration of 15% corresponding to the average number of particles in the lysosomes and their volume concentration. (b) Quantification of CAF1-CCK2 cell death labeled with Annexin V/propidium iodide (AnnV/PI) according to the RMF amplitude (mT) and frequency (Hz). CAF1-CCK2 cells were incubated for 24 h with USPION@gastrin at [Fe] = 16 μg ml^{-1}, washed and exposed to RMF for 2 h. Dead cells were labeled with iFluor488-tagged AnnV/PI, 4 h after magnetic field exposure, and counted by flow cytometry. (c) CAF1-CCK2 and CAF2-CCK2 cells were incubated with USPION@gastrin for 24 h, washed, and exposed or not to RMF (40 mT and 1 Hz) for 2 h. Dead cells were labeled with AnnV/PI and counted 4 h after RMF exposure by flow cytometry. (d) CAF1-CCK2 cells were incubated with USPION@gastrin for 24 h, washed, and exposed or not to static (SMF: 40 mT), alternating (AMF: 40 mT and 1 Hz) or rotating (RMF: 40 mT and 1 Hz) for 2 h. Dead cells were labeled with AnnV/PI and counted 4 h after magnetic field exposure by flow cytometry. (e) and (f) CAF1-CCK2 € and CAF2-CCK2 (f) cells were incubated with USPION@gastrin for 72 h, washed, and exposed or not to RMF (40 mT and 1 Hz) for 2 h, once a day for 6 days. Cell proliferation was evaluated by counting cells 24 h after RMF exposure, for 6 days. Results are expressed as mean ± SEM of at least three separate experiments. Statistical analysis was performed using a one- or two-way ANOVA test.
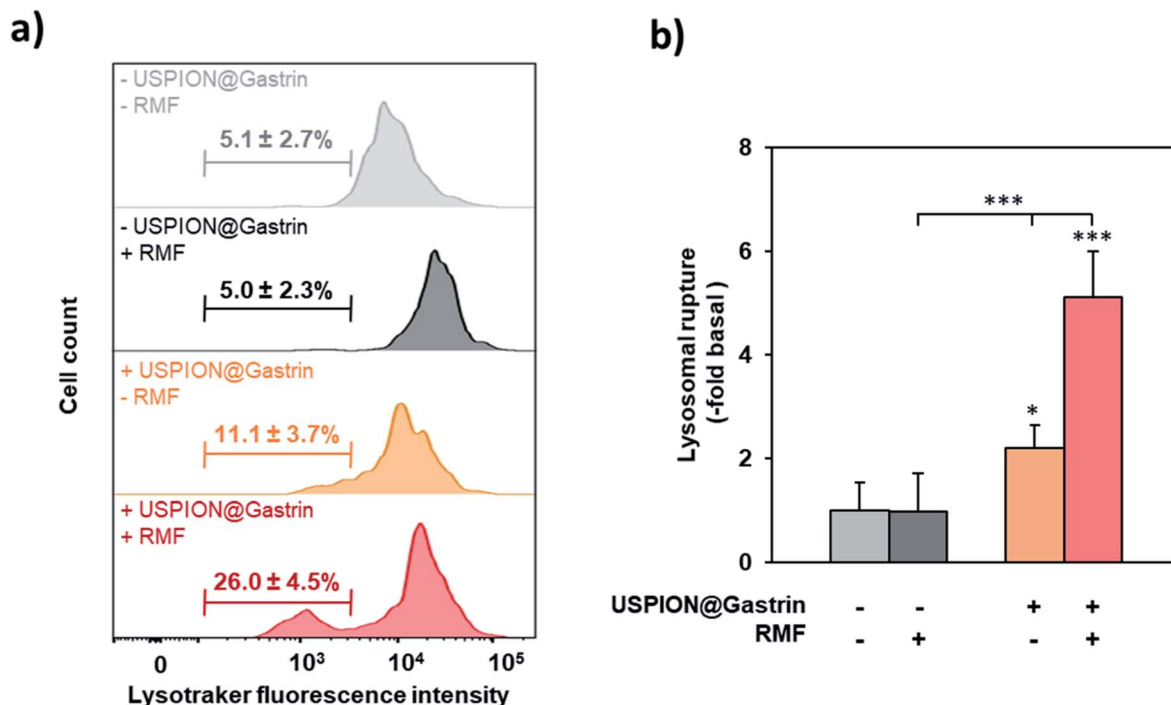
Fig. 5 RMF exposure caused the lysosomal rupture. CAF1-CCK2 cells were incubated with USPION@gastrin at [Fe] = 16 µg ml^{-1} for 24 h, washed, exposed or not to RMF (40 mT and 1 Hz) for 2 h, and then incubated with 10 nM LysoTracker Green. Lysosome integrity was determined by analyzing Lysotracker fluorescence intensity by flow cytometry. (a) Representative peak diagrams of Lysotracker fluorescence intensity determined by flow cytometry. Bars indicate the percentage rate of pale cells with lysosomal rupture revealed by a decreased Lysotracker fluorescence intensity. (b) Quantification of lysosomal rupture was performed by counting the percentage of pale with a decreased Lysotracker fluorescence intensity by flow cytometry images and expressed as a fold change of fluorescence intensity over control cells (in the absence of USPION@gastrin and RMF). Significant difference compared to the control conditions corresponding to cells devoid of USPION@gastrin in the absence of RMF exposure was indicated above the histogram bar. Statistical significances between other conditions are also indicated by lines/brackets. Results are the mean ± SEM of three separate experiments. Statistical analysis was performed using a one-way ANOVA test.

was maintained at 37 °C. While the RMF treatment (40 mT and 1 Hz) had no significant effect on the number of nanoparticle-unloaded cells during the 6 days treatment period when compared to control cells, the proliferation of USPION@gastrin-loaded CAF1-CCK1 and CAF2-CCK2 cells after RMF treatment was significantly ($p < 0.01$) inhibited (Fig. 4e and f). Altogether, these results suggest that the attack on lysosomes *via* RMF activation of lysosome-accumulated USPION@gastrin prompts cell death and affects the growth of the cell population.

RMF induces the rupture of lysosomes containing USPION@gastrin

Since conjugated magnetic nanoparticles with antibodies targeting the lysosomal protein LAMP1 were reported to induce lysosome membrane permeabilization (LMP) under RMF,[31] we determined whether rotating USPION@gastrin nanoparticles, which were accumulated inside CAF-CCK2 lysosomes, caused lysosome damage. CAF1-CCK2 cells were incubated with USPION@gastrin for 24 h, washed to eliminate non-internalized nanoparticles and exposed to RMF for 2 h. Upon staining with Lysotracker, an acidotropic dye that fluorescently labels lysosomes and accumulates in unaltered lysosomes was used to assess the effects of rotating USPION@gastrin on CAF1-CCK2 lysosomal integrity. When lysosome ruptures, the dye

does not accumulate in damaged lysosomes and is released into the cytosol, resulting in a population of cells with reduced fluorescence (pale cells). The decreased Lysotracker fluorescence was measured by flow cytometry. As shown in Fig. 5a and b, cells treated with USPION@gastrin and exposed to RMF show a significant 5.1 ± 0.9-fold increase of the number of pale cells ($26.0 \pm 4.5\%$, $p < 0.001$), as compared to control cells lacking nanoparticles ($5.1 \pm 2.7\%$). No significant effect was observed on CAF1-CCK2 cells lacking USPION@gastrin and exposed to RMF ($5.0 \pm 2.3\%$ of pale cells), as well as on CAF1-CCK2 cells incubated with USPION@gastrin but not exposed to RMF (11.1 ± 3.7 of pale cells). These results indicated that RMF exposure caused lysosome rupture of CAF1-CCK2 cells containing USPION@gastrin.

CAF death induced by USPION@gastrin torque depends on lysosomal cathepsin-B activity

Lysosome rupture is known to result in the leakage of lysosomal enzymes, including cathepsins, into the cytosol leading eventually to cell death. Such a mechanism has been previously identified in response to intra-lysosomal magnetic hyperthermia, due to the release of local thermal energy from nanoparticles accumulated in lysosomes that required cathepsin-B to kill cancer cells.[5] To investigate whether cathepsins could be
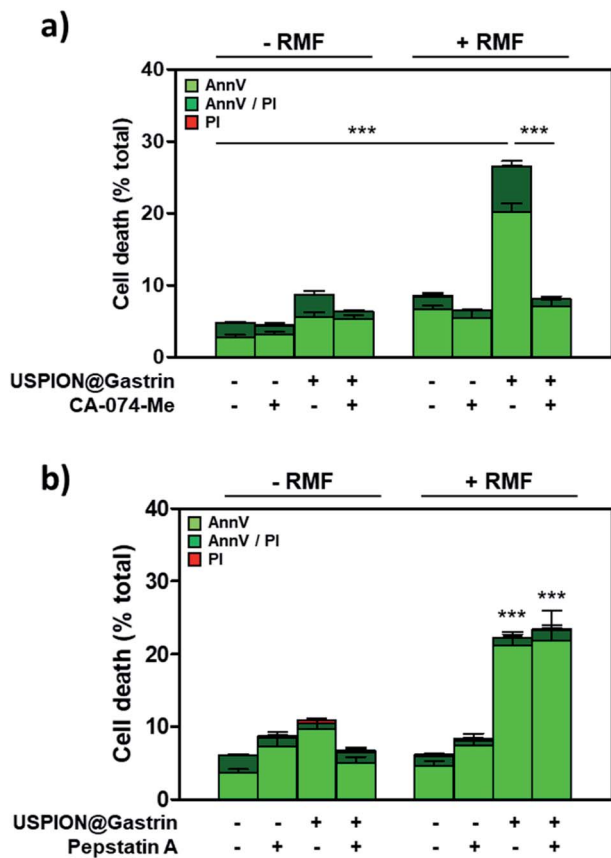
Fig. 6 CAF death induced by USPION@gastrin torque depends on lysosomal cathepsin-B activity. CAF1-CCK2 cells were incubated with USPION@gastrin at [Fe] = 16 µg ml^{-1} for 24 h, washed, exposed or not to RMF (40 mT and 1 Hz) for 2 h in the absence or presence of CA-074-Me (a) or pepstatin A and (b) inhibitors. Dead cells were labeled with AnnV/PI, 4 h after magnetic field exposure, and counted by flow cytometry. Results are expressed as mean ± SEM of at least three separate experiments. Statistical analysis was performed using a one-way ANOVA test.

involved in cell death in response to USPION@gastrin-induced torque, RMF experiments were performed in the presence or in the absence of CA-074-Me, a selective inhibitor of cathepsin-B, or pepstatin A, an inhibitor of aspartyl peptidases including cathepsin-D. After RMF exposure, the cells were cultured under standard conditions for recovery. The impact of treatment was determined by counting dead cells labeled with iFluor488-tagged AnnV and/or PI by flow cytometry, 4 h after RMF exposure (Fig. 6a and b). As shown in Fig. 6a, the effect of USPION@gastrin torque on cell death was totally prevented by CA-074-Me (dead cells: 7.6 ± 0.7% *vs.* 27.5 ± 1.0% in USPION@gastrin-loaded CAF1-CCK2 cells treated in the presence or in the absence of CA-074 Me). In contrast, pepstatin A did not prevent cell death induced by USPION@gastrin torque under RMF (dead cells: 24.4 ± 3.7% *vs.* 22.3 ± 2.0% in USPION@gastrin-loaded CAF1-CCK2 cells treated in the presence or in the absence of pepstatin A, respectively) (Fig. 6b). These results indicate that CAF death induced by USPION@gastrin torque depends on cathepsin-B activity.

Discussion

In the wider context of targeted nanotherapy by magnetic hyperthermia, we explored herein a new strategy consisting in the local release of mechanical energy based on the exposure of targeted 6 nm USPIONs to low-frequency magnetic fields. We first showed that functionalized USPIONs (6 nm iron oxide core) could target the lysosomes of pancreatic cancer-associated fibroblasts (CAFs), a key player in the tumor microenvironment that promotes tumor growth and resistance. Pancreatic CAFs expressing the CCK2 receptor were chosen as a model to obtain the proof-of-concept. Interestingly, such an approach can be developed by targeting other receptors or the protein surface able to internalize. We thus showed that the binding and internalization of USPION@gastrin depend on the presence and the expression level of the CCK2 receptor at the CAF surface, indicating that CAFs overexpressing specific surface receptors can be effectively targeted with functionalized magnetic nanoparticles. Then, we explored the opportunity offered by targeted USPIONs accumulated into CAF lysosomes to act as a therapeutic agent inducing their death upon low-frequency magnetic fields. Here, we aim at discussing the possible mechanisms of cell death, based on the results that we have obtained from magnetic simulations and experiments, and comparing our results with the literature.

An accurate screening of the characteristics of the magnetic field (amplitude, frequency, and type) demonstrated that, using 6 nm diameter USPIONs, cell death is maximized when the field rotates, and its amplitude is around 40 mT and the frequency is around 1 Hz. The former two characteristics (rotation and amplitude) are well predicted and understood by our magnetic simulations. Indeed, we had already theoretically shown that, when the magnetic field rotates instead of being alternating, a much more intense torque is generated in a specific range of magnetic fields.[50] This theoretical behaviour is again illustrated in 4a with the specific parameters of our experiments.

For a relevant comparison of our experimental results with the literature, it should first be recalled that our experiments were performed with single-domain objects, and that our simulations are only valid within this framework. The fact that a rotating field is more efficient than an alternating one has been previously found in the cases where cell death was induced by rather large magnetic objects.[37,40,41] With respect to single-domain objects, Li *et al.* found that increasing the field amplitude in the range [4–20 mT] increased the cell death rate.[32] In contrast, Master *et al.* concluded that the amplitude had no influence on cell viability but with only two AMF amplitudes tested [62 and 125 mT].[35] Thus our result showing that a large magnetic field can be less efficient than a smaller one has, to our knowledge, never been reported. It could appear at first sight counter-intuitive, but it is the natural result of our theoretical mentioned in the previous paragraph. The third characteristic permitting the optimization of cell death – a frequency of 1 Hz – was not predicted by our simulations. In the latter, particles do not move, and it is not surprising that almost no frequency dependence of the torque amplitude is observed:

generally speaking, to see significant changes in the magnetic response of immobilized superparamagnetic nanoparticles, the excitation frequency should be changed by orders of magnitude. Li *et al.* and Chiriac *et al.* studies showed that increasing the frequency in the ranges [0–20 Hz] and [20–50 Hz], respectively, reduced the cell viability, whereas higher frequencies do not induce greater effects [70–100 Hz].[32,41] In our study as well as in others, the optimal frequency able to induce cell death is not the largest one, but rather smaller frequencies ranging from 1 Hz to 50 Hz, which might have a bio-mechanical origin, such as the frequency dependence of the cell response to mechanical stimuli, or such as a resonance effect on the frequency dependence of the mechanical response itself.[32,37,41]

Our magnetic simulations estimated that an assembly of 3000 nanoparticles with a 6 nm crystalline core generate magnetic forces of around 3 pN, a value which is well below the tens to hundreds of pN required to disrupt a bilayer membrane,[18,51] suggesting that lysosome permeabilization or rupture induced by USPION@gastrin torque may involve an alternative mechanism. The mechanical motion or vibration of small magnetic nanoparticles under low frequency magnetic fields has been described to manipulate macromolecules such as DNA (deoxyribonucleic acid) duplexes, enzymes or ion channels.[10,52,53] Interestingly, plasma membrane disturbances induced by magnetic nanoparticle motion were shown to be associated with the activation of ion channels leading to increased levels of intracellular ions (such as calcium, sodium or potassium) and eventually to apoptosis.[27,28,33,39,54] Several ion channels, transient receptor potential ion channels TRPML and two-pores channels TPC, have been identified in endolysosomal compartment whose overexpression in cancers increases cell proliferation, migration, invasion and/or metastasis.[55–57] These channels are osmo-mechanical sensitive as they can be activated by both physical and chemical signals (oxidants, pH, and osmo-mechanical force). Noticeably, the magnetic forces of USPION@gastrin assembly calculated by our simulations – a few pN – are large enough to activate such ion channels.[18] This suggests that the dysregulation of lysosomal ion channels by USPION@gastrin torque may be associated with the impairment of lysosomal ion homeostasis, resulting in lysosome dysfunction and permeabilization and thus cell death.[58,59] While few pN forces generated by the 6 nm nanoparticle assembly conducted to the death of 34% of cells upon 40 mT/1 Hz rotating field application, the nanoparticles design with better anisotropic and magnetic properties to respond to optimized magnetic field parameters may promote the efficiency of magneto-mechanical cell destruction. In addition, nanoparticle surface functionalization (surface charge, size, shape, multiple active targeting…) increasing the nanoparticle uptake by cells may also enhance the efficiency of such a strategy.

Finally, this study highlights first data on the mechanisms at the origin of cell death that involves the lysosome damage and the lysosomal enzyme cathepsin-B. Indeed, we showed that RMF exposure diminished the staining of lysosomes with the pH-independent Lysotracker and that the CA-074-Me inhibitor prevents the effect of RMF on cell death. According to the literature, these results indicate that lysosome permeabilization followed by the leakage of cathepsin-B is likely at the origin of CAF death. Once released into the cytosol, cathepsin-B was shown to activate apoptosis or non-apoptotic cell death pathways.[60] Thus, USPION@gastrin torque under RMF behaved as a lysosomotropic agent in CAF cells and induced cell death through a lysosomal cell death pathway. Among literature data investigating micro- or nanoparticles to induce cell death or tumor regression by mechanical forces, some studies suggested hypotheses about the mechanism of cell death depending on micro- or nano-particle localization. Hence, plasma membrane disruption, lysosome damage or cytoskeleton disorganization have been mentioned to provoke cell death.[30,35,38] Of note, Shen *et al.* showed that the death of glioblastoma cancer cells induced by 62 nm-sized nanocubes under RMF (40 mT and 15 Hz) was associated with lysosome membrane permeabilization.[38] Further studies will allow determining the physical and cellular events leading to cell death. Interestingly, we showed here that such an approach is also efficient on CAFs with ultrasmall superparamagnetic nanoparticles (6 nm core), allowing intravenous injection and making this strategy an interesting therapeutic option to target different cellular components of a tumor by designing nanoparticles to develop multiple targeting strategies. Moreover, our study and others showed that intracellular cell membrane destruction is also efficient to induce cell death compared to the disruption from the cell surface.[27,28,38]

Conclusion

This study establishes a proof-of-concept that targeted 6 nm USPIONs can disrupt the tumor microenvironment through mechanical forces upon rotating magnetic field exposure and opens new opportunities for cancer therapy. We demonstrated that the USPION surface functionalized with gastrin peptide internalized and accumulated into pancreatic CAF lysosomes expressing the CCK2R, chosen as a model, awaiting the identification of a receptor or a set of receptors allowing the targeting of pro-tumoral CAF subpopulations and/or cancer cells. MNP multi-functionalization to target different receptors expressed on the tumor microenvironment and/or cancer cells will be certainly necessary in future preclinical and clinical studies to obtain efficient tumor targeting and therapeutic response. We showed that the CCK2-targeting nanoparticles produce a torque inside lysosomes under a rotating magnetic field, resulting in local mechanical damage of lysosome membranes and effective cell death. After consistent interaction with the lysosome membrane *via* mechanical force or by activating mechanosensitive ion channels on the lysosome membrane under RMF, they efficiently damaged lysosomes, inducing the death of CAFs. Compared to micro-scale magnetic materials, nanomaterials are easily internalized by cells. Moreover, intracellular cell membrane destruction is also efficient to induce cell death compared to plasma membrane disruption. This remote magneto-mechanical actuation approach that can be used to target cancer cells as well as cells from the tumor microenvironment is attractive with the advantage that low-

frequency rotating magnetic fields are safe, penetrate the human body without side effects and could considerably reduce the costs of instrumentation. In the context that the tumor microenvironment has an important role in tumor development, progression and metastasis, as well as in limiting drug penetration and efficacy or resistance, magneto-mechanical depletion of CAF population in tumors offers an interesting adjuvant anti-cancer approach that may increase the efficiency of conventional therapy such as chemotherapy and radiotherapy. Therefore, the present study offers a promising strategy for magnetic nanomedicines to non-invasively treat cancers, in particular cancer presenting a dense tumor microenvironment.

Materials and methods

Chemical materials

Iron(III) acetyl acetonate (>99.9%) and benzyl alcohol (99.8%) were purchased from Sigma Aldrich. Phosphonate – poly(ethylene glycol) PEG – carboxylic acid MW 2500 g mol^{-1} (PO–PEG–COOH) and citrate ions were respectively purchased from Specific Polymers (ref. SP-1P-10-002) and Sigma Aldrich (citrate ions). CA-074-Me and pepstatin A inhibitors were from Sigma Aldrich. The Annexin V Binding Apoptosis Assay Kit was from AAT Bioquest, Inc. (Sunnyvale, CA, USA). LysoTracker® Green DND-26 was from Invitrogen.

Synthesis and functionalization of USPIONs

6 nm USPIONs (ultra-small superparamagnetic iron oxide nanoparticles) were synthesized in benzyl alcohol under microwave heating as reported previously.[45] Briefly, iron(III) acetylacetonate (1.2 mmol) was added to 10 ml of benzyl alcohol and reacted at 210 °C for 30 min under microwave irradiation on a Monowave 300 from Anton Paar. The resulting suspension was extracted from benzyl alcool to water by adding 10 ml of dichloromethane and 10 ml of citrate ions (3.3 mmol) dispersed in water. Immediately after, a phase separation occurs with the transfer of IONPs within the upper water phase. An excess of citrate was removed using an ultrafiltration process (Amicon 30 kDa, Merck Millipore). The coated citrate was removed with NaOH (1 mol l^{-1}) and IONPs were separated using a neodymium magnet. The solid (Fe_3O_4 = 40 mg) was redispersed in water at pH 2 using an HCl solution at 10^{-1} mol l^{-1} and surface functionalized by mixing the solution with a PO–PEG–COOH water solution (pH 2 and 200 mg). Then, the excess of PO–PEG–COOH coating molecules was removed using an ultrafiltration process (Amicon 30 kDa, Merck Millipore) and USPION@PO–PEG–COOH was dispersed in water at pH 7.4 using HCl (10^{-1} mol l^{-1}) and NaOH (10^{-1} mol l^{-1}) solutions.

USPION@PO–PEG–COOH was then decorated with ~30 molecules of a synthetic replicate of gastrin (Cys–Lys–Ser–Ser–Glu–Ala–Tyr–Gly–Trp–Nle–Asp–Phe–NH_2, Covalab) and ~20 molecules of the fluorescent label NHS-DY647-PEG1 (Dyomics GmbH, Jena, Germany), and termed USPION@gastrin. An aliquot of USPION@PO–PEG–COOH was sonicated for 10 min on melting ice (Bioblock Scientific 88154). Firstly, the carboxylic acid functions at the outer surface of IONP@PO–PEG–COOH

were activated using 1-ethyl-3-(3-dimethylaminopropyl) carbodiimide (EDC, 2n COOH) and incubated with ethylenediamine (10n COOH) in MES buffer pH 4.5 at room temperature for 1 h. After 5 washes with 10 volumes of H_2O, the second step was the linkage of fluorophore NHS-DY647-PEG1 (20 molecules per IONP) in phosphate buffer pH 8.3, at room temperature for 1 h. Then, 3-maleimidopropionic acid N-hydroxysuccinimide ester (BMPS, 2n COOH) in solution in DMF was added and incubated at room temperature for 1 h. After 5 washes with 10 volumes of H_2O, gastrin (~100 peptides per nanoparticles) in solution in 30% DMF, 70% H_2O was added to phosphate buffer pH 7.2 and let to react for 2 h. Finally, free maleimide functions were saturated by addition of an excess of cysteine (1000n COOH) to 50 µl of phosphate buffer pH 7.2. After 8 washes with 10 volumes of H_2O, USPION@gastrin was stored at 4 °C.

Physico-chemical characterization of USPIONs

Transmission Electron Microscopy (TEM) samples were prepared by depositing a drop of USPION suspension on carbon coated copper grids placed on a filter paper. TEM images were obtained using a FEI CM10 Microscope (Philips). The median diameter was deduced from TEM data measurements, simulating the diameter distribution with a log-normal function.

The average number of molecules of PO–PEG–COOH per nanocrystal was measured by Fourier Transform Infrared Spectroscopy. Infrared spectra in KBr pellets of various proportions of PO–PEG–COOH mixed with a constant amount of USPIONs were recorded. The normalized 1110 cm^{-1} band was used for the establishment of the calibration curve and the average number of PO–PEG–COOH per nanoparticle was deduced from this curve.

The suspension of USPION@gastrin at 0.1 mg ml^{-1} was prepared in DMEM-F12 containing 0.5% FBS. The suspension was sonicated for 10 min on ice. After temperature equilibrium to 20 °C, the particle size was measured by dynamic light scattering using a Nanotrac 250 (Microtrac, York, PA).

The magnetization curve of USPION@PO-PEG was recorded on a VSM magnetometer (Quantum Design, Versalab) at room temperature. The VSM measured magnetization cycles by applying a field from −3000 to 3000 mT with a sampling rate of approximately 10 mT s^{-1}.

The average number of gastrin derivatives was measured by the OPA method after calibration curve establishment (ESI Fig. S2†). 50 µl of the sample was diluted in 50 µl of NaOH 2 N and left overnight at 60 °C. 1 ml of OPA reagent was added to the mixture and fluorescence measurement was recorded. The average amount of gastrin peptide per nanoparticle was deduced from a calibration. Before use, USPION@gastrin was sonicated on ice for 10 min.

Torque simulations

The magnetic properties of the USPION assembly have been calculated using a kinetic Monte Carlo program.[50] The torque is calculated using monodisperse USPIONs of diameter d = 6 nm, with a uniaxial anisotropy K_{eff} = 13 kJ m^{-3}, displaying a magnetization per unit volume M_s = 500 kA m^{-1} in a rotating

or alternating magnetic field. The magnetic interactions have been made taking into account a sphere containing a disordered assembly of 3000 nanoparticles at a volume concentration of 15% to be the closest of the USPIONs behavior inside a lysosome.

Cell lines

Two immortalized human cancer-associated fibroblast (CAF) cell lines were used. The immortalized human CAF1 line was established by retrovirus-mediated gene transfer of simian virus 40 (SV40) T antigen and human telomerase reverse transcriptase (hTERT) into human pancreatic fibroblasts isolated from the resected pancreas tissue of a patient undergoing operation for pancreatic adenocarcinoma cancer (PDAC), and obtained from Dr A. Masamune (Division of Gastroenterology, Tohoku University Graduate School of Medicine, Japan).[61] The immortalized human CAF2 line was obtained from Dr C. Bousquet's laboratory (INSERM U1037-CRCT, France). CAF2 cells were isolated them from patient tumor tissues of the pancreas surgically resected from PDAC patients, using the outgrowth method as already described,[62] and then immortalized through lentivirus-mediated gene transfer of human telomerase reverse transcriptase (hTERT). Briefly, small tissue blocks were cut (0.5–1 mm^3) using a razor blade and were seeded in 10 cm^2 uncoated culture wells in the presence of DMEM-F12 containing 10% foetal calf de-complemented serum (FBS). Tissue blocks were cultured at 37 °C in a humidified atmosphere at 95% air and 5% CO$_2$. 18 h after seeding, the culture medium was changed. CAFs grew out from the tissue blocks 1 to 3 days later. Fresh patient PDAC samples were obtained after obtaining informed consent in accordance with the declaration of Helsinki and stored at the « Cancer Research Center of Toulouse » collection (CRCT, INSERM U1037, No. CPP DC-2016-2654), according to the French law (declaration to the ministry of higher education and research). This study was approved by the ethic committee of the Institution.

Both cell lines were permanently transfected with the human CCK2 receptor (CCK2R) using the cDNA encoding the CCK2R subcloned in the pcDNA3 vector (BD Biosciences Clontech) and Lipofectamine 2000 (Invitrogen), and clones were selected with 400 μg ml^{-1} Geneticin (Sigma-Aldrich) and termed respectively CAF1-CCK2 and CAF2-CCK2. CAF cells were cultured in a DMEM/F-12 medium (DMEM/F-12 GlutaMAX™, Thermo Fisher Scientific) containing 10% FBS and 100 IU ml^{-1} penicillin/streptomycin (Penicillin–Streptomycin P4333; Sigma Aldrich) in a humidified atmosphere at 95% air and 5% CO$_2$ at 37 °C. CAF1-CCK2 and CAF2-CCK2 cells were grown with 400 μg ml^{-1} Geneticin (Sigma Aldrich).

Analysis of CCK2R expression in CAF cell lines

50×10^3 cells per well were seeded into 24-well plates (Thermo Scientific™) and grown overnight. Cells were incubated with 10 nM Dy647-CCK9 agonist in the presence or in the absence of 10 μM GV 150013X, a specific CCK2 receptor antagonist, for 1 h at 37 °C, in a DMEM/F-12 medium buffered with 10 mM HEPES buffer pH 7.4 containing 0.5% FBS and 100 IU ml^{-1} penicillin–

streptomycin. Then, the cells were rinsed twice with ice-cold PBS containing 0.5% BSA and once with PBS alone. Cells were recovered and transferred to FACS tubes. Cell-associated fluorescence was determined using a BD FACSCalibur™ flow cytometer.

Analysis of cell viability

10^4 cells per well of CAF1-CCK2 and CAF2-CCK2 were plated into 96-well plates (Thermo Scientific™). After overnight growth, the cells were incubated with increased concentrations of USPION@gastrin in a DMEM/F-12 medium buffered with 10 mM HEPES buffer pH 7.4 containing 0.5% FBS and 100 IU ml^{-1} penicillin–streptomycin for 24 h. Cell viability was determined using a MTT viability assay.

Quantification of USPION@gastrin binding and uptake by flow cytometry

10^4 cells per well were seeded into 24-well plates (Thermo Scientific™) and grown overnight. The cells were incubated with USPION@gastrin (2 to 32 μg$_{magnetic Fe}$ ml^{-1}) for 1 to 24 h at 37 °C in a DMEM/F-12 medium buffered with 10 mM HEPES buffer pH 7.4 containing 0.5% FBS and 100 IU ml^{-1} penicillin–streptomycin. For competition experiments, USPION@gastrin (16 μg$_{magnetic Fe}$ ml^{-1}) was incubated in the presence or in the absence of 10 μM gastrin-17, a specific CCK2 receptor agonist, for 24 h at 37 °C. Then, the cells were rinsed twice with ice-cold PBS containing 0.5% BSA and once with PBS alone. The cells were recovered and transferred to FACS tubes. Cell-associated fluorescence was determined using a BD FACSCalibur™ flow cytometer.

USPION@gastrin localization by confocal microscopy

25×10^3 cells per compartment were respectively seeded onto 4-compartment Cellview culture dishes (Greiner Bio-One). After overnight growth, the cells were incubated with USPION@gastrin (16 μg$_{magnetic Fe}$ ml^{-1}) in a DMEM/F-12 medium buffered with 10 mM HEPES buffer pH 7.4 containing 0.5% FBS and 100 IU ml^{-1} penicillin/streptomycin for 24 h. For lysosome staining, the cells were incubated for 15 min in the presence of 10 nM LysoTracker Green DND-26 (excitation: 488 nm, Invitrogen). USPION@gastrin (excitation: 633 nm) and Lysotracker co-localization was analyzed using an LSM780 confocal microscope (Zeiss).

USPION@gastrin localization by transmission electron microscopy

10^4 CAF1-CCK2 cells were grown in 6-dishes plates (Thermo Scientific™) and incubated with USPION@gastrin (16 μg$_{magnetic Fe}$ ml^{-1}) for 24 h. After removing the medium, the cells were fixed with 4% glutaraldehyde in Sorensen buffer for 4 h at 4 °C. The fixed cells were washed with cold Sorensen buffer for 12 h and post-fixed in 1% osmium tetra oxide (osmium 2%, saccharose 0.25 M, and Sorensen 0.05 M) for 1 h at 20 °C, followed by washings with distilled water and uranyl acetate 2% for 12 h at 4 °C. The cells were dehydrated by sequential washings for

10 min in 30, 50, 70 and 95% ethanol followed by 3 washes for 15 min in absolute ethanol. The cells were then embedded in EMBed 812 resin for 12 h. Resin polymerization was obtained at 60 °C for 48 h. Ultrathin sections of 70 nm were prepared, stained with uranyl acetate and lead citrate and examined with a transmission electron microscope (Hitachi HU12A, Japan) operating at 75 kV.

Quantification of USPION@gastrin uptake by using a vibrating sample magnetometer

Magnetic measurements using a vibrating sample magnetometer (PPMS, Quantum Design, USA) were used as a complementary approach to determine the iron content. ∼105 CAF1-CCK1 or CAF2-CCK2 cells were respectively seeded onto 6-well plates at a density and grown for 24 h. The cells were incubated with USPION@gastrin (16 $\mu g_{magnetic\ Fe}$ ml^{-1}) in a DMEM-F12 medium buffered with 10 mM HEPES buffer pH 7.4 containing 0.5% FBS and 100 IU ml^{-1} penicillin–streptomycin for 24 h, at 37 °C in a 5% CO$_2$ atmosphere, and washed twice with ice-cold PBS. The suspension containing a known number of cells was put into a magnetic measurement capsule, the excess of liquid removed, and the remaining liquid was allowed to evaporate. Hysteresis loops were measured at 300 K up to a magnetic field of 5 T. The linear slope corresponding to the diamagnetic signal was removed from raw measurements. The obtained magnetization was divided by the saturation magnetization of the nanoparticles (65 A m^2 kg$_{Fe}^{-1}$) and the number of cells to get the content of iron per cell.

Cell treatment by low magnetic field application and setups

Cell exposure to magnetic fields was performed as follows. CAF1-CCK2 or CAF2-CCK2 cells were seeded into 4-compartment Cellview dishes (Greiner Bio-One) for cell proliferation or cell death analysis respectively, grown overnight and incubated with USPION@gastrin (4, 8 or 16 $\mu g_{magnetic\ Fe}$ ml^{-1}) at 37 °C in a DMEM/F-12 medium buffered with 10 mM HEPES buffer pH 7.4 containing 0.5% FBS and 100 IU ml^{-1} penicillin/ streptomycin. After removing the medium, the cells were rinsed twice with the incubation medium, incubated in the incubation medium and then exposed to a magnetic field. For experiments with a rotating magnetic field (RMF), the setup used is a homemade bench based on a magnet rotated with a motor. The magnet itself is a 2.5 cm thick cylindrical Halbach array magnet with an inner diameter of 6 cm and an outside diameter of 15 cm. Five magnets were elaborated to display different magnetic field amplitudes. Different amplitudes (20, 40, 60, 200, and 380 mT) and frequencies (0.2, 1, 5, 10, and 20 Hz) were assayed. The magnetic field amplitude varies weakly with the position at the scale of the Cellview dish, as shown by space-dependent magnetic field measurements: for the magnet rated as "380 mT" and "40 mT" the magnetic field equals 380 ± 50 mT and 41 ± 1 mT, respectively. The rotating magnet is surrounded by a Plexiglas chamber, the temperature inside which is regulated using a fan able to blow heated air. For experiments with a static magnetic field (SMF), this first setup is used without magnet rotation. For the comparison between

RMF and AMF, a second home-made setup is used. In this second setup, the magnetic field is generated by an ensemble of 6 laminated silicon iron magnetic poles surrounded by copper wires in a configuration resembling one of the stators. The sample space has a diameter of 4.5 cm. Depending on the phase of the current sent into the coils surrounding the poles, either a rotating magnetic field or an alternating one is generated. The temperature inside the sample space and the coil is regulated using a similar device to the previous magnetic field generator. In all these experiments, the temperature of the Cellview dish was maintained at 37.0 ± 0.2 °C during magnetic field exposure. At the end of the experiments, the cells were placed in a humidified atmosphere at 5% CO$_2$ and 37 °C.

Determination of cell death

25×10^3 cells per compartment of CAF1-CCK2 or CAF2-CCK2 cells were seeded into 4-compartment Cellview dishes (Greiner Bio-One) for cell proliferation or cell death analysis respectively, grown overnight and incubated with USPION@-gastrin (4, 8 or 16 $\mu g_{magnetic\ Fe}$ ml^{-1}) for 24 h at 37 °C in a DMEM/F-12 medium buffered with 10 mM HEPES buffer pH 7.4 containing 0.5% FBS and 100 IU ml^{-1} penicillin/ streptomycin. After removing the medium, the cells were rinsed twice with the incubation medium, incubated in the incubation medium with or without 10 μM CA-074 Me or 10 μM pepstatin A for 1 h, and then exposed to a magnetic field for 2 h. The effects of magnetic field treatments were investigated by labeling dead cells with Annexin V-iFluor488 (AnnV) and propidium iodide (PI) (excitation: 488 and 540 nm respectively, AAT Bioquest), 4 h after magnetic field exposure and counting them using a BD FACSCalibur™ flow cytometer.

Cell proliferation analysis

10×10^3 cells per compartment of CAF1-CCK2 or CAF2-CCK2 cells were seeded into 4-compartment Cellview dishes (Greiner Bio-One) for cell proliferation or cell death analysis respectively, grown overnight and incubated with USPION@-gastrin (4, 8 or 16 $\mu g_{magnetic\ Fe}$ ml^{-1}) for 72 h at 37 °C in a DMEM/F-12 medium buffered with 10 mM HEPES buffer pH 7.4 containing 0.5% FBS and 100 IU ml^{-1} penicillin/ streptomycin. After removing the medium, the cells were rinsed twice with the incubation medium, and then exposed to a magnetic field for 2 h once per day. The effects of magnetic field treatments were investigated on cell proliferation by counting the cell number by using a cell counter (Beckman cell counter z2) after 24 h of RMF treatment. Cells were counted once per day for 6 days.

Lysosomal membrane permeabilization

CAF1-CCK2 and CAF2-CCK2 cells having internalized USPION@gastrin were exposed to low frequency RMF for 2 h, incubated with a DMEM-F12 medium 0.5% FBS containing 10 nM LysoTracker Green DND-26 (Invitrogen, excitation wavelength: 488 nm) for 15 minutes, and rinsed with the incubation medium. Lysosome integrity was determined by

analyzing Lysotracker fluorescence intensity by flow cytometry using a BD FACSCalibur™ flow cytometer.

Statistical analysis

Results are expressed as the mean ± SEM of at least three independent experiments. Statistical analysis was performed using a one- or two-way ANOVA test. Differences were considered significant when $p < 0.05$.

Author contributions

Sara Lopez: investigation and formal analysis. Nicolas Hallali: investigation and formal analysis. Yoann Lalatonne: investigation, formal analysis, and writing – review & editing. Arnaud Hillion: investigation, formal analysis, and writing – original draft. Joana C Antunes: investigation and formal analysis. Nizar Serhan: investigation and formal analysis. Pascal Clerc: investigation, visualization, and formal analysis. Daniel Fourmy: writing – review & editing. Laurence Motte: supervision, funding acquisition, writing – original draft, and writing – review & editing. Julian Carrey: supervision, funding acquisition, writing – original draft, and writing – review & editing. Véronique Gigoux: supervision, funding acquisition, writing – original draft, and writing – review & editing.

Conflicts of interest

The authors declare no conflict of interest.

Acknowledgements

References

1 I. Hilger and W. A. Kaiser, Iron oxide-based nanostructures for MRI and magnetic hyperthermia, *Nanomedicine*, 2012, **7**(9), 1443–1459.

2 Y. X. Wang, S. M. Hussain and G. P. Krestin, Superparamagnetic iron oxide contrast agents: physicochemical characteristics and applications in MR imaging, *Eur. Radiol.*, 2001, **11**(11), 2319–2331.

3 M. H. Schwenk, Ferumoxytol: a new intravenous iron preparation for the treatment of iron deficiency anemia in patients with chronic kidney disease, *Pharmacotherapy*, 2010, **30**(1), 70–79.

4 E. A. Perigo, G. Hemery, O. Sandre, D. Ortega, E. Garaio, F. Plazaola and F. J. Teran, Fundamentals and advances in magnetic hyperthermia, *Appl. Phys. Rev.*, 2015, **2**(4), 041302.

5 P. Clerc, P. Jeanjean, N. Hallali, M. Gougeon, B. Pipy, J. Carrey, D. Fourmy and V. Gigoux, Targeted Magnetic Intra-Lysosomal Hyperthermia produces lysosomal reactive oxygen species and causes Caspase-1 dependent cell death, *J. Controlled Release*, 2018, **270**, 120–134.

6 M. Creixell, A. C. Bohorquez, M. Torres-Lugo and C. Rinaldi, EGFR-targeted magnetic nanoparticle heaters kill cancer cells without a perceptible temperature rise, *ACS Nano*, 2011, **5**(9), 7124–7129.

7 M. Domenech, I. Marrero-Berrios, M. Torres-Lugo and C. Rinaldi, Lysosomal membrane permeabilization by targeted magnetic nanoparticles in alternating magnetic fields, *ACS Nano*, 2013, **7**(6), 5091–5101.

8 C. Sanchez, D. El Hajj Diab, V. Connord, P. Clerc, E. Meunier, B. Pipy, B. Payre, R. P. Tan, M. Gougeon, J. Carrey, V. Gigoux and D. Fourmy, Targeting a G-protein-coupled receptor overexpressed in endocrine tumors by magnetic nanoparticles to induce cell death, *ACS Nano*, 2014, **8**(2), 1350–1363.

9 S. Carregal-Romero, P. Guardia, X. Yu, R. Hartmann, T. Pellegrino and W. J. Parak, Magnetically triggered release of molecular cargo from iron oxide nanoparticle loaded microcapsules, *Nanoscale*, 2015, **7**(2), 570–576.

10 H. Huang, S. Delikanli, H. Zeng, D. M. Ferkey and A. Pralle, Remote control of ion channels and neurons through magnetic-field heating of nanoparticles, *Nat. Nanotechnol.*, 2010, **5**(8), 602–606.

11 M. Yamaguchi, A. Ito, A. Ono, Y. Kawabe and M. Kamihira, Heat-Inducible Gene Expression System by Applying Alternating Magnetic Field to Magnetic Nanoparticles, *ACS Synth. Biol.*, 2014, **3**(5), 273–279.

12 J. Kolosnjaj-Tabi, R. Di Corato, L. Lartigue, I. Marangon, P. Guardia, A. K. A. Silva, N. Luciani, O. Clement, P. Flaud, J. V. Singh, P. Decuzzi, T. Pellegrino, C. Wilhelm and F. Gazeau, Heat-Generating Iron Oxide Nanocubes: Subtle "Destructurators" of the Tumoral Microenvironment, *ACS Nano*, 2014, **8**(5), 4268–4283.

13 J. Kolosnjaj-Tabi, I. Marangon, A. Nicolas-Boluda, A. K. A. Silva and F. Gazeau, Nanoparticle-based hyperthermia, a local treatment modulating the tumor extracellular matrix, *Pharmacol. Res.*, 2017, **126**, 123–137.

14 I. Hilger, *In vivo* applications of magnetic nanoparticle hyperthermia, *Int. J. Hyperthermia*, 2013, **29**(8), 828–834.

15 S. Dutz and R. Hergt, Magnetic particle hyperthermia—a promising tumour therapy?, *Nanotechnology*, 2014, **25**(45), 452001.

16 M. Johannsen, B. Thiesen, P. Wust and A. Jordan, Magnetic nanoparticle hyperthermia for prostate cancer, *Int. J. Hyperthermia*, 2010, **26**(8), 790–795.

17 K. Maier-Hauff, F. Ulrich, D. Nestler, H. Niehoff, P. Wust, B. Thiesen, H. Orawa, V. Budach and A. Jordan, Efficacy and safety of intratumoral thermotherapy using magnetic iron-oxide nanoparticles combined with external beam radiotherapy on patients with recurrent glioblastoma multiforme, *J. Neuro-Oncol.*, 2011, **103**(2), 317–324.

18 Y. I. Golovin, S. L. Gribanovsky, D. Y. Golovin, N. L. Klyachko, A. G. Majouga, A. M. Master, M. Sokolsky and A. V. Kabanov, Towards nanomedicines of the future: Remote magneto-mechanical actuation of nanomedicines by alternating magnetic fields, *J. Controlled Release*, 2015, **219**, 43–60.

19 R. J. Mannix, S. Kumar, F. Cassiola, M. Montoya-Zavala, E. Feinstein, M. Prentiss and D. E. Ingber, Nanomagnetic actuation of receptor-mediated signal transduction, *Nat. Nanotechnol.*, 2008, **3**(1), 36–40.

20 A. Tay, A. Kunze, C. Murray and D. Di Carlo, Induction of Calcium Influx in Cortical Neural Networks by Nanomagnetic Forces, *ACS Nano*, 2016, **10**(2), 2331–2341.

21 D. Kilinc, C. L. Dennis and G. U. Lee, Bio-Nano-Magnetic Materials for Localized Mechanochemical Stimulation of Cell Growth and Death, *Adv. Mater.*, 2016, **28**(27), 5672–5680.

22 Z. G. Forbes, B. B. Yellen, D. S. Halverson, G. Fridman, K. A. Barbee and G. Friedman, Validation of high gradient magnetic field based drug delivery to magnetizable implants under flow, *IEEE Trans. Biomed. Eng.*, 2008, **55**(2), 643–649.

23 T. Mizuki, N. Watanabe, Y. Nagaoka, T. Fukushima, H. Morimoto, R. Usami and T. Maekawa, Activity of an enzyme immobilized on superparamagnetic particles in a rotational magnetic field, *Biochem. Biophys. Res. Commun.*, 2010, **393**(4), 779–782.

24 C. Naud, C. Thebault, M. Carriere, Y. X. Hou, R. Morel, F. Berger, B. Dieny and H. Joisten, Cancer treatment by magneto-mechanical effect of particles, a review, *Nanoscale Adv.*, 2020, **2**(9), 3632–3655.

25 A. Plan Sangnier, S. Preveral, A. Curcio, A. K. A. Silva, C. T. Lefevre, D. Pignol, Y. Lalatonne and C. Wilhelm, Targeted thermal therapy with genetically engineered magnetite magnetosomes@RGD: Photothermia is far more efficient than magnetic hyperthermia, *J. Controlled Release*, 2018, **279**, 271–281.

26 S. Richard, M. Boucher, Y. Lalatonne, S. Meriaux and L. Motte, Iron oxide nanoparticle surface decorated with cRGD peptides for magnetic resonance imaging of brain tumors, *Biochim. Biophys. Acta, Gen. Subj.*, 2017, **1861**(6), 1515–1520.

27 D. H. Kim, E. A. Rozhkova, I. V. Ulasov, S. D. Bader, T. Rajh, M. S. Lesniak and V. Novosad, Biofunctionalized magnetic-vortex microdiscs for targeted cancer-cell destruction, *Nat. Mater.*, 2010, **9**(2), 165–171.

28 M. F. Contreras, R. Sougrat, A. Zaher, T. Ravasi and J. Kosel, Non-chemotoxic induction of cancer cell death using magnetic nanowires, *Int. J. Nanomed.*, 2015, **10**, 2141–2153.

29 Y. Chen, P. Han, Y. Wu, Z. Zhang, Y. Yue, W. Li and M. Chu, Hedgehog-Like Gold-Coated Magnetic Microspheres that Strongly Inhibit Tumor Growth through

Magnetomechanical Force and Photothermal Effects, *Small*, 2018, **14**(45), e1802799.

30 Y. Cheng, M. E. Muroski, D. Petit, R. Mansell, T. Vemulkar, R. A. Morshed, Y. Han, I. V. Balyasnikova, C. M. Horbinski, X. Huang, L. Zhang, R. P. Cowburn and M. S. Lesniak, Rotating magnetic field induced oscillation of magnetic particles for *in vivo* mechanical destruction of malignant glioma, *J. Controlled Release*, 2016, **223**, 75–84.

31 E. M. Zhang, M. F. Kircher, M. Koch, L. Eliasson, S. N. Goldberg and E. Renstrom, Dynamic Magnetic Fields Remote-Control Apoptosis *via* Nanoparticle Rotation, *ACS Nano*, 2014, **8**(4), 3192–3201.

32 W. Li, Y. Liu, Z. Qian and Y. Yang, Evaluation of Tumor Treatment of Magnetic Nanoparticles Driven by Extremely Low Frequency Magnetic Field, *Sci. Rep.*, 2017, **7**, 46287.

33 H. Ju, Y. Cui, Z. Chen, Q. Fu, M. Sun and Y. Zhou, Effects of combined delivery of extremely low frequency electromagnetic field and magnetic Fe3O4 nanoparticles on hepatic cell lines, *Am. J. Transl. Res.*, 2016, **8**(4), 1838–1847.

34 A. Vegerhof, E. A. Barnoy, M. Motiei, D. Malka, Y. Danan, Z. Zalevsky and R. Popovtzer, Targeted Magnetic Nanoparticles for Mechanical Lysis of Tumor Cells by Low-Amplitude Alternating Magnetic Field, *Materials*, 2016, **9**(11), 943.

35 A. M. Master, P. N. Williams, N. Pothayee, R. Zhang, H. M. Vishwasrao, Y. I. Golovin, J. S. Riffle, M. Sokolsky and A. V. Kabanov, Remote Actuation of Magnetic Nanoparticles For Cancer Cell Selective Treatment Through Cytoskeletal Disruption, *Sci. Rep.*, 2016, **6**, 33560.

36 S. Du, J. Li, C. Du, Z. Huang, G. Chen and W. Yan, Overendocytosis of superparamagnetic iron oxide particles increases apoptosis and triggers autophagic cell death in human osteosarcoma cell under a spinning magnetic field, *Oncotarget*, 2017, **8**(6), 9410–9424.

37 W. Wong, W. L. Gan, N. Liu and W. S. Lew, Magneto-actuated cell apoptosis by biaxial pulsed magnetic field, *Sci. Rep.*, 2017, **7**(1), 10919.

38 Y. Shen, C. Wu, T. Q. P. Uyeda, G. R. Plaza, B. Liu, Y. Han, M. S. Lesniak and Y. Cheng, Elongated Nanoparticle Aggregates in Cancer Cells for Mechanical Destruction with Low Frequency Rotating Magnetic Field, *Theranostics*, 2017, **7**(6), 1735–1748.

39 W. Wong, W. L. Gan, Y. K. Teo and W. S. Lew, Interplay of cell death signaling pathways mediated by alternating magnetic field gradient, *Cell Death Discovery*, 2018, **4**, 49.

40 K. Spyridopoulou, A. Makridis, N. Maniotis, N. Karypidou, E. Myrovali, T. Samaras, M. Angelakeris, K. Chlichlia and O. Kalogirou, Effect of low frequency magnetic fields on the growth of MNP-treated HT29 colon cancer cells, *Nanotechnology*, 2018, **29**(17), 175101.

41 H. Chiriac, E. Radu, M. Tibu, G. Stoian, G. Ababei, L. Labusca, D. D. Herea and N. Lupu, Fe-Cr-Nb-B ferromagnetic particles with shape anisotropy for cancer cell destruction by magneto-mechanical actuation, *Sci. Rep.*, 2018, **8**(1), 11538.

42 K. P. Olive, M. A. Jacobetz, C. J. Davidson, A. Gopinathan, D. McIntyre, D. Honess, B. Madhu, M. A. Goldgraben, M. E. Caldwell, D. Allard, K. K. Frese, G. Denicola, C. Feig, C. Combs, S. P. Winter, H. Ireland-Zecchini, S. Reichelt, W. J. Howat, A. Chang, M. Dhara, L. Wang, F. Ruckert, R. Grutzmann, C. Pilarsky, K. Izeradjene, S. R. Hingorani, P. Huang, S. E. Davies, W. Plunkett, M. Egorin, R. H. Hruban, N. Whitebread, K. McGovern, J. Adams, C. Iacobuzio-Donahue, J. Griffiths and D. A. Tuveson, Inhibition of Hedgehog signaling enhances delivery of chemotherapy in a mouse model of pancreatic cancer, *Science*, 2009, **324**(5933), 1457–1461.

43 R. F. Hwang, T. Moore, T. Arumugam, V. Ramachandran, K. D. Amos, A. Rivera, B. Ji, D. B. Evans and C. D. Logsdon, Cancer-associated stromal fibroblasts promote pancreatic tumor progression, *Cancer Res.*, 2008, **68**(3), 918–926.

44 C. Duluc, S. Moatassim-Billah, M. Chalabi-Dchar, A. Perraud, R. Samain, F. Breibach, M. Gayral, P. Cordelier, M. B. Delisle, M. P. Bousquet-Dubouch, R. Tomasini, H. Schmid, M. Mathonnet, S. Pyronnet, Y. Martineau and C. Bousquet, Pharmacological targeting of the protein synthesis mTOR/4E-BP1 pathway in cancer-associated fibroblasts abrogates pancreatic tumour chemoresistance, *EMBO Mol. Med.*, 2015, **7**(6), 735–753.

45 S. Richard, V. Eder, G. Caputo, C. Journe, P. Ou, J. Bolley, L. Louedec, E. Guenin, L. Motte, N. Pinna and Y. Lalatonne, USPIO size control through microwave nonaqueous sol-gel method for neoangiogenesis T-2 MRI contrast agent, *Nanomedicine*, 2016, **11**(21), 2769–2779.

46 S. Richard, V. Eder, G. Caputo, C. Journe, P. Ou, J. Bolley, L. Louedec, E. Guenin, L. Motte, N. Pinna and Y. Lalatonne, USPIO size control through microwave nonaqueous sol-gel method for neoangiogenesis T2 MRI contrast agent, *Nanomedicine*, 2016, **11**(21), 2769–2779.

47 M. J. Berna, O. Seiz, J. F. Nast, D. Benten, M. Blaker, J. Koch, A. W. Lohse and A. Pace, CCK1 and CCK2 receptors are expressed on pancreatic stellate cells and induce collagen production, *J. Biol. Chem.*, 2010, **285**(50), 38905–38914.

48 J. P. Smith, T. K. Cooper, C. O. McGovern, E. L. Gilius, Q. Zhong, J. Liao, A. A. Molinolo, J. S. Gutkind and G. L. Matters, Cholecystokinin receptor antagonist halts progression of pancreatic cancer precursor lesions and fibrosis in mice, *Pancreas*, 2014, **43**(7), 1050–1059.

49 A. Mohammed, N. B. Janakiram, C. Suen, N. Stratton, S. Lightfoot, A. Singh, G. Pathuri, R. Ritchie, V. Madka and C. V. Rao, Targeting cholecystokinin-2 receptor for pancreatic cancer chemoprevention, *Mol. Carcinog.*, 2019, **58**(10), 1908–1918.

50 J. Carrey and N. Hallali, Torque undergone by assemblies of single-domain magnetic nanoparticles submitted to a rotating magnetic field, *Phys. Rev. B*, 2016, **94**(18), 184420.

51 R. Afrin, T. Yamada and A. Ikai, Analysis of force curves obtained on the live cell membrane using chemically modified AFM probes, *Ultramicroscopy*, 2004, **100**(3–4), 187–195.

52 A. A. Nikitin, A. Y. Yurenya, T. S. Zatsepin, I. O. Aparin, V. P. Chekhonin, A. G. Majouga, M. Farle, U. Wiedwald and M. A. Abakumov, Magnetic Nanoparticles as a Tool for Remote DNA Manipulations at a Single-Molecule Level, *ACS Appl. Mater. Interfaces*, 2021, **13**(12), 14458–14469.

53 L. D. Knecht, N. Ali, Y. Wei, J. Z. Hilt and S. Daunert, Nanoparticle-mediated remote control of enzymatic activity, *ACS Nano*, 2012, **6**(10), 9079–9086.

54 T. N. Zamay, G. S. Zamay, I. V. Belyanina, S. S. Zamay, V. V. Denisenko, O. S. Kolovskaya, T. I. Ivanchenko, V. L. Grigorieva, I. V. Garanzha, D. V. Veprintsev, Y. E. Glazyrin, A. V. Shabanov, V. Y. Prinz, V. A. Seleznev, A. E. Sokolov, V. S. Prokopenko, P. D. Kim, A. Gargaun, M. V. Berezovski and A. S. Zamay, Noninvasive Microsurgery Using Aptamer-Functionalized Magnetic Microdisks for Tumor Cell Eradication, *Nucleic Acid Ther.*, 2017, **27**(2), 105–114.

55 M. Xu and X. P. Dong, Endolysosomal TRPMLs in Cancer, *Biomolecules*, 2021, **11**(1), 65.

56 C. C. Chen, E. Krogsaeter and C. Grimm, Two-pore and TRP cation channels in endolysosomal osmo-/mechanosensation and volume regulation, *Biochim. Biophys. Acta, Mol. Cell Res.*, 2021, **1868**(2), 118921.

57 X. Zhang, M. Hu, Y. Yang and H. Xu, Organellar TRP channels, *Nat. Struct. Mol. Biol.*, 2018, **25**(11), 1009–1018.

58 M. B. Morelli, C. Amantini, D. Tomassoni, M. Nabissi, A. Arcella and G. Santoni, Transient Receptor Potential Mucolipin-1 Channels in Glioblastoma: Role in Patient's Survival, *Cancers*, 2019, **11**(4), 525.

59 G. A. Colletti, M. T. Miedel, J. Quinn, N. Andharia, O. A. Weisz and K. Kiselyov, Loss of lysosomal ion channel transient receptor potential channel mucolipin-1 (TRPML1) leads to cathepsin B-dependent apoptosis, *J. Biol. Chem.*, 2012, **287**(11), 8082–8091.

60 A. Serrano-Puebla and P. Boya, Lysosomal membrane permeabilization in cell death: new evidence and implications for health and disease, *Ann. N. Y. Acad. Sci.*, 2016, **1371**(1), 30–44.

61 S. Hamada, A. Masamune, T. Takikawa, N. Suzuki, K. Kikuta, M. Hirota, H. Hamada, M. Kobune, K. Satoh and T. Shimosegawa, Pancreatic stellate cells enhance stem cell-like phenotypes in pancreatic cancer cells, *Biochem. Biophys. Res. Commun.*, 2012, **421**(2), 349–354.

62 M. G. Bachem, E. Schneider, H. Gross, H. Weidenbach, R. M. Schmid, A. Menke, M. Siech, H. Beger, A. Grunert and G. Adler, Identification, culture, and characterization of pancreatic stellate cells in rats and humans, *Gastroenterology*, 1998, **115**(2), 421–432.